Receptor-Targeted Nanoparticles for *In vivo* Imaging of Breast Cancer

Lily Yang,[1,2,4] Xiang-Hong Peng,[1] Y. Andrew Wang,[6] Xiaoxia Wang,[2] Zehong Cao,[1] Chunchun Ni,[2] Prasanthi Karna,[1] Xinjian Zhang,[5] William C. Wood,[1,4] Xiaohu Gao,[3] Shuming Nie,[3,4] and Hui Mao[2,4]

Abstract

Purpose: Cell-surface receptor-targeted magnetic iron oxide nanoparticles provide molecular magnetic resonance imaging contrast agents for improving specificity of the detection of human cancer.

Experimental Design: The present study reports the development of a novel targeted iron oxide nanoparticle using a recombinant peptide containing the amino-terminal fragment of urokinase-type plasminogen activator (uPA) conjugated to magnetic iron oxide nanoparticles amino-terminal fragment conjugated-iron oxide (ATF-IO). This nanoparticle targets uPA receptor, which is overexpressed in breast cancer tissues.

Results: ATF-IO nanoparticles are able to specifically bind to and be internalized by uPA receptor–expressing tumor cells. Systemic delivery of ATF-IO nanoparticles into mice bearing s.c. and i.p. mammary tumors leads to the accumulation of the particles in tumors, generating a strong magnetic resonance imaging contrast detectable by a clinical magnetic resonance imaging scanner at a field strength of 3 tesla. Target specificity of ATF-IO nanoparticles showed by *in vivo* magnetic resonance imaging is further confirmed by near-IR fluorescence imaging of the mammary tumors using near-IR dye-labeled amino-terminal fragment peptides conjugated to iron oxide nanoparticles. Furthermore, mice administered ATF-IO nanoparticles exhibit lower uptake of the particles in the liver and spleen compared with those receiving nontargeted iron oxide nanoparticles.

Conclusions: Our results suggest that uPA receptor–targeted ATF-IO nanoparticles have potential as molecularly targeted, dual modality imaging agents for *in vivo* imaging of breast cancer.

Authors' Affiliations: Departments of [1]Surgery, [2]Radiology, and [3]Biomedical Engineering, [4]Winship Cancer Institute, Emory University School of Medicine; [5]Department of Chemistry, Georgia State University, Atlanta, Georgia; and [6]Ocean Nanotech, LLC, Springdale, Arkansas

Received 12/22/08; revised 3/6/09; accepted 3/27/09; published OnlineFirst 7/7/09.

Grant support: Emory-Georgia Tech Nanotechnology Center for Personalized and Predictive Oncology of the NIH National Cancer Institute (NCI) Center of Cancer Nanotechnology Excellence (U54 CA119338), NIH NCI R01 CA133722 (L. Yang), Emory Molecular and Translational Imaging Center grant (NIH, NCI, P50CA128613), Seed Grant from EmTech Bio, Inc. (H. Mao), the Friends for An Early Breast Cancer Test Foundation, the Idea Award of the Breast Cancer Research Program of the Department of Defense (BC021952), and the Nancy Panoz Endowed Chair (L. Yang). The costs of publication of this article were defrayed in part by the payment of page charges. This article must therefore be hereby marked *advertisement* in accordance with 18 U.S.C. Section 1734 solely to indicate this fact.

Note: L. Yang and X-H. Peng contributed equally to the studies in this article.

Current address for X. Gao: Department of Bioengineering, University of Washington, Seattle, Washington.

Requests for reprints: Lily Yang, Department of Surgery and Winship Cancer Institute, Emory University School of Medicine, C-4088, 1365 C Clifton Road NE, Atlanta, GA 30322. Phone: 404-778-4269; Fax: 404-778-5530; E-mail: Lyang02@emory.edu or Hui Mao, Department of Radiology, Emory Center for Systems Imaging, Emory University School of Medicine, 1841 Clifton Road, Atlanta, GA 30329. Phone: 404-712-0357; Fax: 404-712-5948; E-mail: hmao@emory.edu.

doi:10.1158/1078-0432.CCR-08-3289

Breast cancer is the most common type of cancer and the second leading cause of cancer-related death among women. Novel approaches for the detection of primary and metastatic breast cancers are urgently needed to increase the survival of patients. A promising strategy to improve the specificity and sensitivity of cancer imaging is to use biomarker target–specific imaging probes (1–3) for image-based diagnosis and treatment monitoring. Currently, targeted radionuclide probes have been used for cancer detection by positron emission tomography or single photon emission tomography (2, 4, 5). Although nuclear imaging modalities show a high sensitivity, they lack good resolution and anatomic localization of the tumor lesion and require complicated and expensive radiochemistry. In addition, the half-life of the radiotracer often limits the ability for dynamic and time-resolved imaging and may not be able to capture the biomarker-targeting agent to reach and accumulate in the tumor. Magnetic resonance imaging offers a high spatial resolution and three-dimensional anatomic details and has been widely used in clinical oncology imaging. Recently, breast magnetic resonance imaging was recommended by the American Cancer Society as a screening approach, adjunct to mammography, for the early detection of breast cancer in women at high risk for this disease (6). Although breast cancer magnetic resonance imaging shows a

Translational Relevance

Breast cancer is the most common cancer in women with about 180,000 new cases and 40,000 deaths each year in the United States. Currently, breast magnetic resonance imaging is used for early detection of breast cancer and is recommended as a routine screen for women at high risk for the disease. Although breast magnetic resonance imaging using a nontargeted contrast agent has a relatively high sensitivity in detecting lesions, it lacks specificity in determining the pathologic characteristics of the lesions. Recent studies show that patients receiving magnetic resonance imaging have a higher rate of biopsy and mastectomy compared with those without this imaging procedure. Magnetic resonance imaging is a promising noninvasive imaging approach for preoperative staging of breast cancer and monitoring tumor response to therapy. Therefore, the development of biomarker-targeted magnetic resonance imaging contrast probes that increase the specificity of breast cancer magnetic resonance imaging should have a great impact on the detection and treatment of breast cancer.

high sensitivity in detecting small breast lesions, a major challenge is its low specificity when using a nontargeted contrast agent such as gadolinium chelates, resulting in a high false-positive rate and unnecessary biopsy and mastectomy (7). Therefore, the development of molecularly targeted magnetic resonance imaging contrast agents may increase the specificity of magnetic resonance imaging, as well as provide information on the level of biomarker expression in breast cancers.

Recently, biocompatible and functionalized nanoparticles have been shown to target tumors and produce optical, magnetic, and/or radioactive signals for enhancing sensitivity and specificity of noninvasive tumor imaging. Previous studies have shown the feasibility of producing such imaging probes for *in vivo* magnetic resonance imaging of cancers (8–10). The unique features of nanoparticles that make them suitable for receptor-targeted imaging include (*a*) having a prolonged blood retention time and (*b*) providing reactive function groups and a large surface area for loading large numbers or multiple types of tumor-targeting ligands. However, several issues remain to be addressed in making nanoparticle imaging probes for clinical applications. These include the identification and availability of suitable imaging biomarkers, the delivery of sufficient amount of probe *in vivo*, and the development of imaging probes with sufficient signal amplification and contrast enhancement (11).

Paramagnetic iron oxide nanoparticles can induce remarkably strong magnetic resonance imaging contrast and have a large surface area and versatile surface chemistry for surface functionalization and the introduction of biomolecules (12–14). Their biological safety in humans has been tested, with nontargeted iron oxide nanoparticles currently in use to detect liver tumor lesions or lymph node metastases in patients (15, 16). Previous attempts to develop targeted iron oxide nanoparticles used dextran or polyethylene glycol–coated iron oxide to conjugate targeting ligands and showed the feasibility and improved sensitivity and specificity of such biomarker-targeted magnetic resonance imaging nanoprobes (3, 14, 17–19). However, most of these ligands were directed to molecular targets that were expressed only in a small percentage of tumor tissues or subpopulations of tumor cells, such as HER-2/*neu*, transferrin, mucin 1, and folate acid, which limits the sensitivity and application for molecularly targeted cancer imaging in patients.

In this study, we used the amino-terminal fragment of the high affinity receptor binding domain of urokinase-type plasminogen activator (uPA) to target its cellular receptor, which is up-regulated in a high percentage of tumor cells and tumor-associated stromal cells, such as endothelial cells, macrophages, and fibroblasts, of many human cancer types (20–23). It is well known that the interaction of uPA with its cellular receptor results in conversion of plasminogen to serine protease, a central regulator of the activation of other proteases, including matrix metalloproteinase, which promotes tumor metastasis and angiogenesis. An elevated level of uPA receptor is associated with tumor aggressiveness, the presence of distant metastasis, and poor prognosis in breast cancer patients (24–28). In human breast cancer tissues, high levels of uPA receptor are detected in 54% of ductal carcinoma *in situ* and in 60% to 90% of invasive breast cancer tissues (24, 29).

To achieve optimal tumor targeting and imaging, we have developed novel paramagnetic iron oxide nanoparticles that have uniform core sizes and are functionalized through surface coating of ampiphilic polymers. This surface coating provides a stable hydrophobic protective inner layer around a single crystal of iron oxide nanoparticle with carboxylate groups in the outer layer readily available for conjugation with amino-terminal fragment peptides. Amino-terminal fragment conjugated-iron oxide (ATF-IO) nanoparticles specifically bind to and are internalized by uPA receptor–expressing cells. We showed that systemic delivery of ATF-IO nanoparticles into mice bearing mammary tumors led to the accumulation of the targeted nanoparticles in subcutaneous (s.c.) and metastatic mammary tumors, inducing magnetic resonance imaging contrast changes sufficient for *in vivo* tumor imaging. By conjugation of Cy5.5, a near-IR dye, to the amino-terminal fragment peptides, we were able to achieve *in vivo* tumor imaging with magnetic resonance imaging and optical imaging.

Materials and Methods

Breast cancer cell lines

Mouse mammary carcinoma cell line 4T1 stably expressing a firefly luciferase gene was obtained from Dr. Mark W. Dewhirst at Duke University (Durham, NC). Human breast cancer cell line T47D was purchased from American Type Culture Collection.

Preparation of amino-terminal fragment–iron oxide nanoparticles

A cDNA fragment encoding amino acids 1 to 135 of mouse uPA, isolated by PCR amplification using a PCR primer pair containing forward (5′-CACCATGGGCAGTGTACTTGGAGCTCC-3′) and reverse (5′-GCTAAGAGAGCAGTCA-3′) primers, was cloned into pET101/D-TOPO expression vector (Invitrogen). Recombinant amino-terminal fragment peptides were expressed in *Escherichia coli* BL21 (Invitrogen) and purified from bacterial extracts under native conditions using a Ni^{2+} nitrilotriacetic acid (NTA)-agarose column (Qiagen). Purification efficiency was determined by SDS-PAGE and >95% of purified proteins were amino-terminal fragment peptides. Cy5.5 maleimide (GE Healthcare), a near-IR dye, was conjugated to amino-terminal fragment peptides using the manufacturer's protocol. Nontargeted dye molecules were separated from the Cy5.5 dye–labeled amino-terminal fragment peptides using Sephadex G25 column.

Paramagnetic iron oxide nanoparticles were prepared as described (30) using iron oxide powder as the iron precursor, oleic acid as the ligand, and octadecene as the solvent. The core size and hydrodynamic size of the iron oxide nanoparticles were measured using transmission electron microscopy and light scattering scan, respectively. The particles were coated with amphiphilic polymers using a similar method, as reported previously (31). Amino-terminal fragment peptides were conjugated to the surface of iron oxide nanoparticles via cross-linking of carboxyl groups to amino side groups on the amino-terminal fragment peptides, as shown in Fig. 1. Briefly, the polymer-coated iron oxide nanoparticles were activated with ethyl-3-dimethyl amino propyl carbodiimide (Pierce) and sulfo-N-hydroxysuccinimide for 15 min. After purification using Nanosep 100k OMEGA (Pall Corp.), activated iron oxide nanoparticles were reacted with amino-terminal fragment or Cy5.5 – amino-terminal fragment peptides at a molar ratio iron oxide to amino-terminal fragment of 1:20 in PBS (pH 7.0) at 4°C overnight, generating amino-terminal fragment – iron oxide or Cy5.5 – amino-terminal fragment – iron oxide nanoparticles. The final amino-terminal fragment – iron oxide conjugates were purified using Nanosep 100k column filtration. Conjugation efficiency of amino-terminal fragment peptides to the iron oxide nanoparticles was confirmed by the measurement of fluorescence intensity of Cy5.5 – amino-terminal fragment – iron oxide nanoparticles using fluorescence spectroscopy and the ζ potential change before and after conjugation of the amino-terminal fragment ligands to iron oxide nanoparticles. The number of amino-terminal fragment peptides conjugated to each iron oxide nanoparticle was estimated by measuring the fluorescence intensity of a diluted sample of Cy5.5 – amino-terminal fragment – iron oxide nanoparticles using an emission wavelength of 696 nm and then comparing the value to a linear standard curve prepared using various concentrations of Cy5.5 – amino-terminal fragment peptides.

Western blot analysis

Western blot analysis was done as described using a standard protocol in our laboratory (32). To confirm the presence of amino-terminal fragment peptides in SDS/PAGE gel, the protein was transferred to polyvinylidene difluoride membranes (Bio-Rad laboratories). An anti – His tag monoclonal antibody (Novagen) was used to identify the His-tagged amino-terminal fragment-peptides. After reacting with horseradish peroxidase – labeled rat anti – mouse immunoglobulin G antibody, the amino-terminal fragment peptide band was detected by enhanced chemiluminescence using ECL Plus (GE Healthcare) followed by autoradiography. The level of uPA receptor was determined using an anti – uPA receptor polyclonal rabbit antibody (Santa Cruz Biotechnology) that reacts with mouse and human uPA receptor and horseradish peroxidase – conjugated goat anti – rabbit immunoglobulin G. The protein bands were detected using ECL.

Ni-NTA-agarose pull-down assays

To determine whether the purified recombinant amino-terminal fragment peptides, either free or conjugated to iron oxide nanoparticles, bind to uPA receptor, we did a combined pull-down and Western blot analysis. Ni^{2+}-NTA-agarose beads were incubated with His-tagged amino-terminal fragment peptides or amino-terminal fragment – iron oxide nanoparticles at 4°C for 30 min. The conjugated beads were washed twice with binding buffer and incubated with 500 μg of total cell lysate obtained from 4T1 or T47D cells for 2 h. Bound proteins were eluted from the beads using elution buffer containing 400 mmol/L imidazole and then examined by Western Blot analysis to determine the amount of uPA receptor pulled down by amino-terminal fragment – or amino-terminal fragment – iron oxide – conjugated Ni-NTA agarose beads in each sample, as described above.

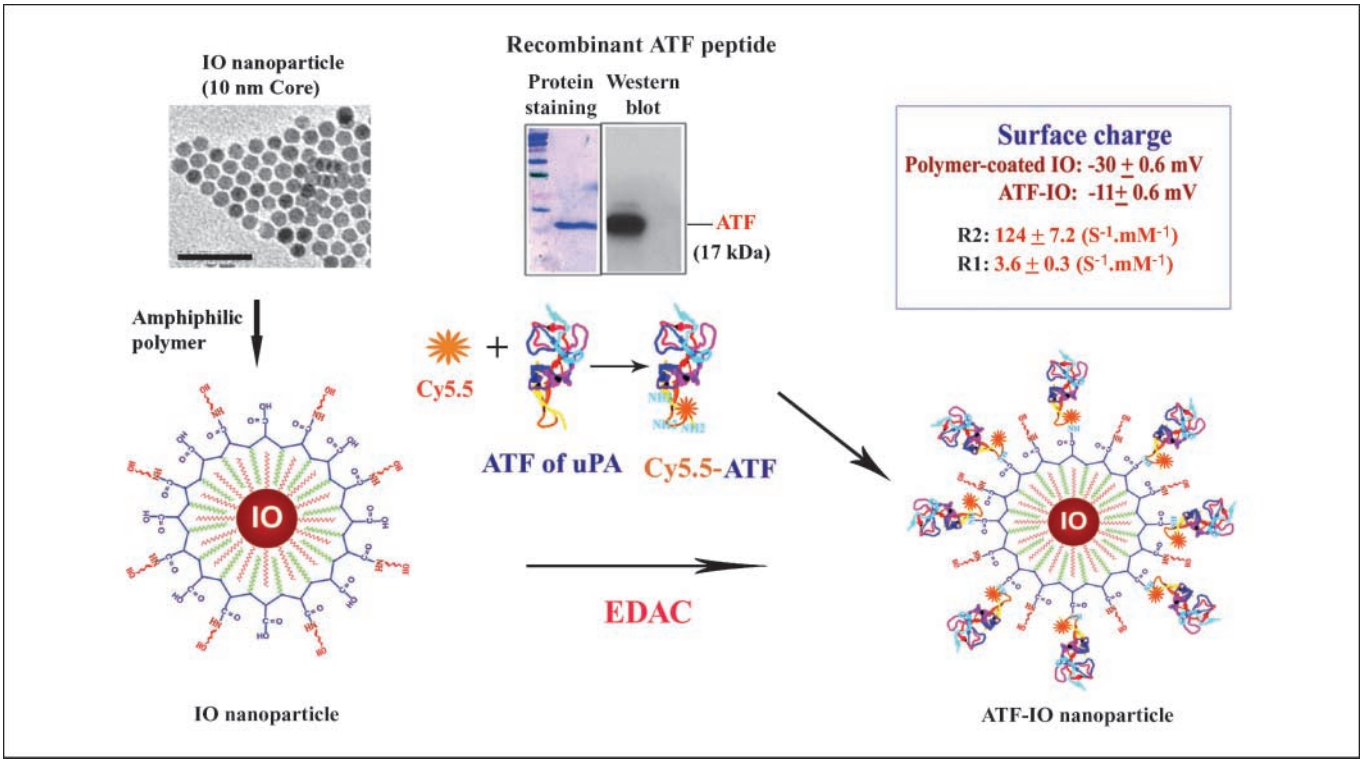

Fig. 1. Characteristics of ATF-IO nanoparticles. Uniform-size IO nanoparticles have a 10-nm core size as shown by transmission electron microscopy and are coated with amphiphilic copolymers modified with short polyethylene glycol chains (scale bar: 50 nm). The purity of recombinant amino-terminal fragment (ATF) peptides was confirmed by Coomassie blue staining of SDS-PAGE gel and by Western blotting using an anti – His tag antibody. Cy5.5 maleimide was conjugated to ATF peptides through a bond between maleimide esters and free thiol groups of cystidine residues of the ATF peptide. ATF or Cy5.5 – ATF peptides were then conjugated to IO nanoparticles via the carboxyl groups mediated by ethyl-3-dimethyl amino propyl carbodiimide (EDAC).

Immunofluorescence labeling

Acetone-fixed frozen normal breast and cancer tissue sections were incubated with 5 μg/mL of polyclonal rabbit anti–uPA receptor antibody, followed by biotinylated goat anti–rabbit immunoglobulin G. After further incubation with Texas-red avidin, the slides were examined under a fluorescence microscope (Zeiss Axioplan with Axiovision software, Carl Zeiss MicroImaging, Inc.). To detect the level of uPA receptor expression in living cancer cells, cells were incubated with an anti–uPA receptor antibody at 4°C for 30 min. After incubation with FITC–goat anti–rabbit immunoglobulin G, cells were examined under the fluorescence microscope.

Specificity of ATF-IO nanoparticles to cancer cells

Cells cultured on glass chamber slides (Nalge Nunc International) were incubated with 13.5 pmol of Cy 5.5–ATF-IO or nontargeted iron oxide nanoparticles at 37°C for 3 h. After washing with PBS, the slides were examined under a confocal microscope (Perkin Elmer Ultraview ERS, PerkinElmer Life and Analytic Sciences, Inc.). To localize the iron oxide nanoparticles, the cells incubated with Cy5.5–ATF-IO or iron oxide nanoparticles were fixed with 4% formaldehyde in PBS and stained with Prussian blue staining by incubating the cells with a 1:1 mixture of 5% potassium ferrocyanide and 5% HCl acid for 30 min at 37°C to confirm the presence of iron oxide nanoparticles (33).

In vitro magnetic resonance imaging scan

Cells were incubated with serum-free medium containing nontargeted iron oxide or ATF-IO nanoparticles at 37°C for 3 h. After washing with PBS, the cells were embedded in 0.8% agarose in 24-well plates. Plates were then scanned in a 3-T magnetic resonance imaging scanner (Philips Medical System) using a T_1-weighted gradient echo sequence and a multi-echo T_2–weighted fast spin echo sequence, which simultaneously collects a series of data points at different echo times (i.e., 20 echo time (TE) points from 10-200 ms with a 10 ms interval) for T_2 relaxometry measurement.

Mouse mammary tumor models

S.c. tumor model. Mouse mammary tumor 4T1 cells were injected s.c. into the back flank area of 6- to 8-wk-old female BALB/c or nude mice. We used nude mice for optical imaging to reduce background fluorescence.

Intraperitoneal (i.p.) metastatic mammary tumor model. 4T1 cells stably transfected with a firefly luciferase gene were directly injected into the upper right side of the peritoneal cavity. Tumor growth was monitored by bioluminescence imaging using the Xenogen bioluminescence imaging system (Xenogen Corp.).

In vivo *magnetic resonance imaging of mouse mammary tumors.* Tumor-bearing mice were examined using a 3-T magnetic resonance imaging scanner (Philips Medical System), with a customized rodent coil to obtain magnetic resonance images. Because magnetic resonance imaging contrast effect is greatly dependent on the magnetic field strength (34), we chose to test the feasibility of detecting iron oxide nanoparticle–induced contrast at a clinically relevant field strength (3 T), with consideration of the potential application of this imaging probe in patients. Animals were anesthetized by i.p. injection of a ketamine-xylazine mixture (95:5 mg/kg). Animals were kept warm in the scanner using warm pads. A set of survey images was obtained using T_2-weighted fast spin echo imaging sequence with repetition time (TR) of 5,000 ms and TE of 120 ms. This was followed by high resolution imaging in the coronal view (i.e., slices cut through from head to tail), with a field of view of 110 × 40 mm, imaging matrix of 256 × 192 (reconstructed to 356 × 256), and 40 slices with 1.1-mm slice thickness without slice gap.

The imaging sequences included T_1- and T_2-weighted spin echo or gradient echo methods and the three-dimensional fast-spoiled gradient echo technique. A TE of 10 ms and TR of 350 ms were used for T_1-weighted spin echo imaging, and TE of 50 ms and TR of 1,500 ms were used for T_2-weighted fast spin echo imaging. A multi-echo T_2 weighted fast spin echo sequence with 12 TEs (range, 10-120 ms; a 10 ms interval) was used to obtain T_2 maps of the whole mouse. The mice were injected with various nanoparticles suspended in PBS, through the tail vein and then scanned at different time points. For postcontrast scan, care was taken to maintain the same animal positions and use same imaging sequences and parameters across different scan sessions. Images from pre- and postcontrast administration were compared to evaluate the efficacy of contrast enhancement. Multi-echo T_2 images of slices were used for calculating T_2 maps using a home-developed program based on Matlab (The Mathworks, Inc.). Because iron oxide nanoparticles typically induced T_2-weighted contrast change, the signal reduction in T_2-weighted imaging and change in the T_2 value were used to follow and estimate the accumulation of nontargeted or targeted iron oxide nanoparticles in the area. Region of interest analysis was used to evaluate and quantify the contrast agent–induced changes in magnetic resonance imaging signal or T_2 value in the tumor and other selected tissues and organs. Regions of interest of tumors were drawn based on the tumor T_2-signal enhancement in T_2-weighted images or at a long TE time point (TE, 80 ms) in multi-TE T_2-mapping imaging.

Near-IR optical imaging of mouse mammary tumors

Tumor-bearing mice were placed on an alfalfa-free rodent diet (Teklad 2918, Harlan Teklad) to reduce background fluorescence. Near-IR images of the tumor-bearing mice were taken using the Kodak *in vivo* FX imaging system (Carestream Molecular Imaging) before and at different time points after the nanoparticle injection. For each near-IR image, a corresponding X-ray image was taken to provide anatomic registration of the tumor.

Histologic analysis

Tumor and normal tissues were collected from the mice at the end of *in vivo* imaging experiments. Five-micrometer frozen tissue sections were incubated with Prussian blue staining solution to confirm the presence of iron oxide nanoparticles in the tissue sections.

Results

Characterization of ATF-IO nanoparticles. The magnetic iron oxide nanoparticles synthesized for this study have a 10-nm core size. We coated the nanoparticles with a monolayer of amphiphilic polymers grafted with carbon alkyl side chains to stabilize and functionalize their surface, resulting in an estimated 18-nm water-soluble iron oxide nanoparticle with carboxyl side groups. To reduce nonspecific binding and uptake by normal tissues, short polyethylene glycol chains were conjugated to a portion of the carboxyl side groups on the amphiphilic polymers. Our results showed that magnetic iron oxide nanocrystal used in this study has a strong T_1- and T_2-shortening effect with R_1 (e.g., $1/T_1$) = 3.6 ± 0.3/(mmol/L)/s and R_2 ($1/T_2$) = 124 ± 7.2/(mmol/L)/s at 3 T (Fig. 1). Such amphiphilic polymer–coated iron oxide nanoparticles have combined characteristics of a relatively small particle size for easy *in vivo* delivery, a large surface area for conjugating biomolecules, and sufficient T_2 effect for magnetic resonance imaging contrast.

The amount and purity of recombinant mouse amino-terminal fragment peptides were determined by gel electrophoresis and Western blot analysis. Coomassie blue staining of the SDS-PAGE gel revealed an amino-terminal fragment band located at ~17 kDa (Fig. 1). The presence of His-tagged amino-terminal fragment peptides was confirmed by Western blot using a monoclonal anti–His tag antibody, showing a strong positive band in the location corresponding to the amino-terminal fragment-peptides identified by Coomassie blue staining (Fig. 1). Conjugation of amino-terminal fragment peptides to

the negatively charged carboxyl groups on the particle surface was further confirmed by the reduction of surface potential from an average of -30 mV to -11 mV after attachment of amino-terminal fragment peptides, suggesting the charge neutralization of carboxyl groups after conjugation with peptides (Fig. 1). From the measurement of fluorescence intensity produced from the Cy5.5 dye conjugated to the ATF-IO nanoparticles, we estimated that 8 to 10 amino-terminal fragment peptides were attached to each nanoparticle (Fig. 1).

Specific binding and internalization of ATF-IO nanoparticles to uPA receptor–expressing mammary tumor cells. We examined the level of uPA receptor expression in human breast cancer and normal tissues. A high level of surface uPA receptor was found in mouse mammary tumor 4T1 cells by immunofluorescence labeling of viable cells using an anti–uPA receptor antibody. On the other hand, human breast cancer T47D cells that lack uPA receptor expression were used as a negative control in this study (Fig. 2A). Consistent with previous observations, uPA receptor is strongly expressed in invasive breast cancer tissues but is not detected in normal breast tissues (ref. 24; Fig. 2A).

To determine whether amino-terminal fragment peptides maintain a high binding affinity after being conjugated to the iron oxide nanoparticles, we did a pull-down assay using cell lysates obtained from uPA receptor–positive 4T1 and –negative T47D cells. Our results showed that free amino-terminal fragment peptides and ATF-IO nanoparticles bound to and precipitated uPA receptor proteins in the cell lysates, resulting in a positive uPA receptor band detected by Western blot assay in 4T1 but not T47D cell lysates (Fig. 2B). It has been shown that interaction of uPA with uPA receptor leads to the internalization of the ligand/receptor complex (35). To determine whether the binding of amino-terminal fragment to uPA receptor leads to receptor-mediated endocytosis, we examined 4T1 and T47D cells after incubation with Cy5.5–ATF-IO at 37°C for 3 hours under a confocal microscope. We found that Cy5.5–ATF-IO nanoparticles were internalized by 4T1 cells but not by T47D cells (Fig. 2C). The presence of intracellular iron oxide nanoparticles in 4T1 cells was further shown by Prussian blue staining (Fig. 2C).

Binding and internalization of ATF-IO nanoparticles in tumor cells and magnetic resonance imaging contrast effect. Receptor-mediated binding and internalization of imaging probes promote their accumulation at the tumor site, which increases contrast effect. Prussian blue staining detected a high level of iron oxide nanoparticles in 4T1 cells incubated with ATF-IO but not with nontargeted iron oxide nanoparticles. uPA receptor–negative T47D cells showed only a very low level of nonspecific uptake (Fig. 3A). 4T1 cells incubated with ATF-IO nanoparticles showed magnetic resonance imaging contrast with signal reduction in T_2-weighted gradient echo imaging (Fig. 3B, *top*). T_2 relaxometry measurements indicated that the T_2 value of 4T1 cells bound with ATF-IO nanoparticles dropped significantly compared with those of the T47D cells incubated with ATF-IO oxide nanoparticles and the samples treated with nontargeted iron oxide nanoparticles (Fig. 3B, *bottom*). Because the T_2 value is a function of the iron concentration, the T_2 relaxometry data suggest that reduction of T_2 relaxation time and magnetic resonance imaging signal in T_2 weighted imaging are induced by the specific binding of ATF-IO nanoparticles to the uPA receptor–expressing 4T1 cells.

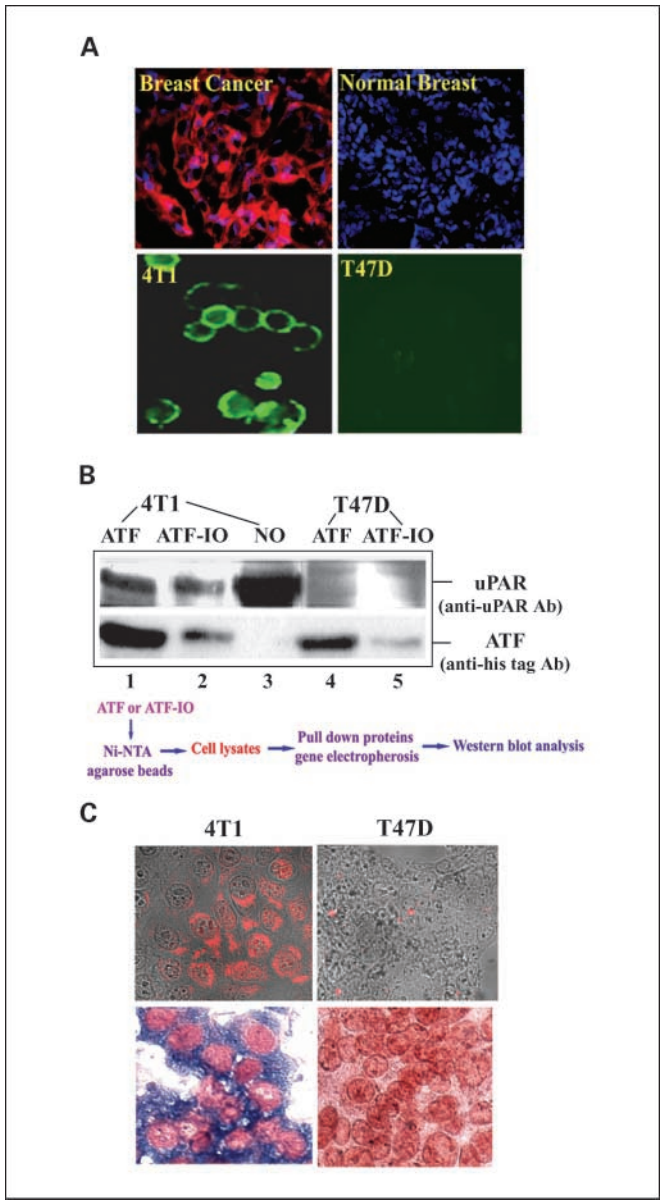

Fig. 2. Specificity of amino-terminal fragment peptides or ATF-IO nanoparticles. *A,* immunofluorescence labeling. A high level of urokinase plasminogen activator receptor (*red*) is detected in frozen tissue sections of invasive human breast cancer tissues but not in normal breast tissue obtained from the same patient (*top*). Blue, Hoechst 33342 background staining. Surface labeling of viable cells using anti–urokinase plasminogen activator receptor antibody shows a high level of urokinase plasminogen activator receptor in 4T1 cells but not in T47D cells (*green, bottom*). *B,* immunoprecipitation assay. Lane 1, free amino-terminal fragment (ATF) peptides pulled down urokinase plasminogen activator receptor (uPAR) protein from 4T1 cell lysates; lane 2, ATF-IO nanoparticles are also capable of binding and pulling (uPAR) protein; lane 3, control total lysates of 4T1 cells; lanes 4 and 5, the uPAR protein band is not detected after incubation of free ATF peptides (*lane 4*) or ATF-IO nanoparticles (*lane 5*) with T47D cell lysates. *C,* specific binding and internalization of Cy5.5–ATF-IO nanoparticles in urokinase plasminogen activator receptor–expressing tumor cells. Confocal images show intracellular localization of Cy5.5 fluorescence (*red*) in 4T1 but not in T47D cells (*top*). Prussian blue staining further confirms the presence of blue iron staining inside the 4T1 cells (*bottom*).

In vivo *targeting and magnetic resonance imaging of s.c. mammary tumors in mice.* In BALB/c mice bearing s.c. mouse mammary tumors derived from the 4T1 tumor cell line, T_2-weighted gradient echo imaging and multi-echo fast spin

echo imaging showed that ATF-IO nanoparticles selectively accumulated in tumors, as evidenced by a reduction in T_2 values and signal decrease in T_2-weighted images in various areas of the tumor mass (Fig. 4A). The region of interest analysis of magnetic resonance imaging signal change showed a 3-fold signal reduction in animals receiving ATF-IO nanoparticles when compared with that in mice receiving nontargeted iron oxide particles (Fig. 4B). Although we observed decreases in magnetic resonance imaging signals in the liver and spleen in the mice injected with ATF-IO nanoparticles because of an iron oxide particle–induced T_2 effect, the reduction in magnetic resonance imaging signal was 50% (liver) to 80% (spleen) less than that in mice that received nontargeted iron oxide nanoparticles, suggesting that liver and spleen uptake of the nanoparticles was reduced for ATF-IO nanoparticles (Fig. 4B). To further confirm the distribution of nontargeted and ATF-IO nanoparticles in normal and tumor tissues, Prussian blue staining was done on tissue sections obtained from the mice that received control iron oxide or ATF-IO nanoparticles. Prussian blue–stained cells were detected in the tumor sections of animals that received ATF-IO nanoparticles but not in sections from animals that received nontargeted iron oxide nanoparticles. High magnification images showed the intracellular localization of iron oxide nanoparticles in the cells (Fig. 4C). In normal tissues, we found high levels of Prussian blue–positive cells in the liver and spleen of the mice that received nontargeted iron oxide nanoparticles. However, liver and spleen tissue sections from the group receiving ATF-IO nanoparticles had fewer positive cells. We did not detect iron oxide nanoparticles in the tissue sections of the brain or heart from mice injected with either nontargeted iron oxide or ATF-IO nanoparticles (Fig. 4C). For both groups, the lung and kidney tissues were also negative in most cases (Fig. 4C) and only a few scattered iron-positive cells were detected in some sections.

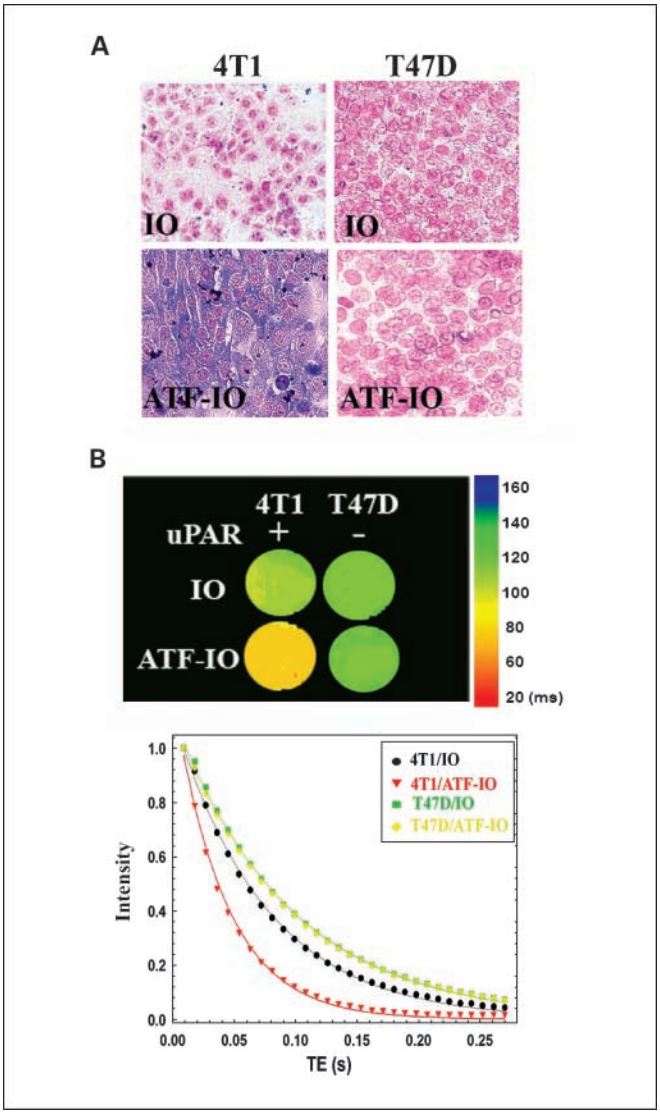

Fig. 3. ATF-IO nanoparticle – induced magnetic resonance imaging signal change after binding to tumor cells. *A,* Prussian blue staining shows specific binding and internalization of ATF-IO nanoparticles in 4T1 cells. A low level of scattered blue staining is found in 4T1 cells incubated with nontargeted iron oxide nanoparticles or urokinase plasminogen activator receptor – negative T47D cells incubated with either iron oxide (IO) or ATF-IO nanoparticles. *B,* reduction of T_2 values in 4T1 cells (*top*) but not in T47D cells measured by magnetic resonance imaging T_2 relaxometry implies the specific binding of ATF-IO nanoparticles to urokinase plasminogen activator receptor – expressing cells. A low T_2 value (*orange-to-red color*) correlates with a high iron concentration. The fastest T_2 value drop was detected in 4T1 cells incubated with ATF-IO nanoparticles (*bottom, red curve*). Scale bar, echo time (TE) in milliseconds. T_2 values of each sample/well were calculated from multi-echo images by fitting the decay curve on a pixel-by-pixel basis using the nonlinear mono-exponential algorithm of $M_i = M_0 * \exp(-TEi/T_2)$. M_i is the intensity or magnitude of the measurement at a time point of *i*. M_0 is the intensity or magnitude of the measurement at the time of zero.

Targeted magnetic resonance imaging of i.p. mammary tumor lesions using ATF-IO nanoparticles. We tested the feasibility of targeting and *in vivo* imaging of metastatic lesions using an animal model bearing i.p. 4T1 tumors. The presence and development of the 4T1 tumor was determined and followed by bioluminescence imaging (36). At 5 hours after injection of the ATF-IO nanoparticles, magnetic resonance imaging signals decreased in two tumor lesions located on top of the right kidney (Fig. 5, *top*). The magnetic resonance imaging signal in the region recovered gradually 30 hours after the injection of the ATF-IO nanoparticles. In contrast, we did not detect an iron oxide nanoparticle-induced magnetic resonance imaging signal change in a tumor-bearing mouse after injection of nontargeted iron oxide (Fig. 5, *bottom*). The selective accumulation of uPA receptor–targeted ATF-IO nanoparticles in this metastatic i.p. tumor model was further confirmed by Prussian blue staining of tissue sections from the sacrificed animals. A high percentage of iron-positive cells was found in the tumor lesion, whereas the kidney beneath the tumor was negative (Fig. 5, *top*). On the other hand, we did not detect iron-positive cells in tissue sections of the i.p. tumor mass obtained from the mouse that received nontargeted iron oxide nanoparticles, whereas the adjacent normal liver tissue had a high level of iron-positive cells (Fig. 5, *bottom*).

Validation of tumor-targeted magnetic resonance imaging in 4T1 mouse mammary tumors using near-IR optical imaging. Near-IR optical imaging provides a simple and sensitive approach to confirm tumor targeting and to monitor the distribution of Cy5.5–ATF-IO nanoparticles in small animals. When monitoring mice bearing s.c. 4T1 tumors at different time points after injection of Cy5.5–ATF-IO nanoparticles, we observed a strong near-IR signal in the tumor mass 24 hours after administration of the nanoparticles. The signal intensity in the tumor mass increased to a peak level at 48 hours but declined at 72 hours (Fig. 6A). We also detected near-IR signals in kidneys,

suggesting that some Cy5.5–ATF-IO nanoparticle and/or Cy5.5–amino-terminal fragment dissociated from iron oxide nanoparticles may be eliminated through the kidney. Furthermore, we found that areas with magnetic resonance imaging contrast change in the tumor overlapped well with the presence of near-IR signal when comparing optical and magnetic resonance images (Fig. 6B). Examination of the tissue sections with positive Prussian blue staining revealed that Cy5.5 near-IR signals colocalized with blue iron-positive cells (Fig. 6C).

Reduced nonspecific uptake of amino-terminal fragment–iron oxide nanoparticles. Previous studies reported that iron oxide nanoparticles can be nonspecifically taken up by macrophages, as well as the reticuloendothelial system in the liver and spleen. We examined the tumor tissue sections stained with both Prussian blue and an antibody to CD68, a marker for macrophages (37). We found iron-positive cells present in CD68-positive and -negative cell populations. A high percentage of iron-positive cells did not express CD68, suggesting that nonmacrophage cell types such as tumor cells contain iron oxide nanoparticles. It has been shown that active macrophages in breast cancer tissues also express a high level of uPA receptor (21, 38). It is possible that the presence of iron-positive macrophages may be due to active targeting of uPA receptor–expressing macrophages rather than nonspecific uptake of iron oxide nanoparticles.

Additionally, a magnetic resonance imaging T_2 map of a mammary tumor showed that accumulation of amino-terminal fragment–iron oxide nanoparticles was not uniformly distributed inside the tumor mass. At various sections of tumor magnetic resonance images, magnetic resonance imaging signal decreases were heterogeneous in the tumor, suggesting that

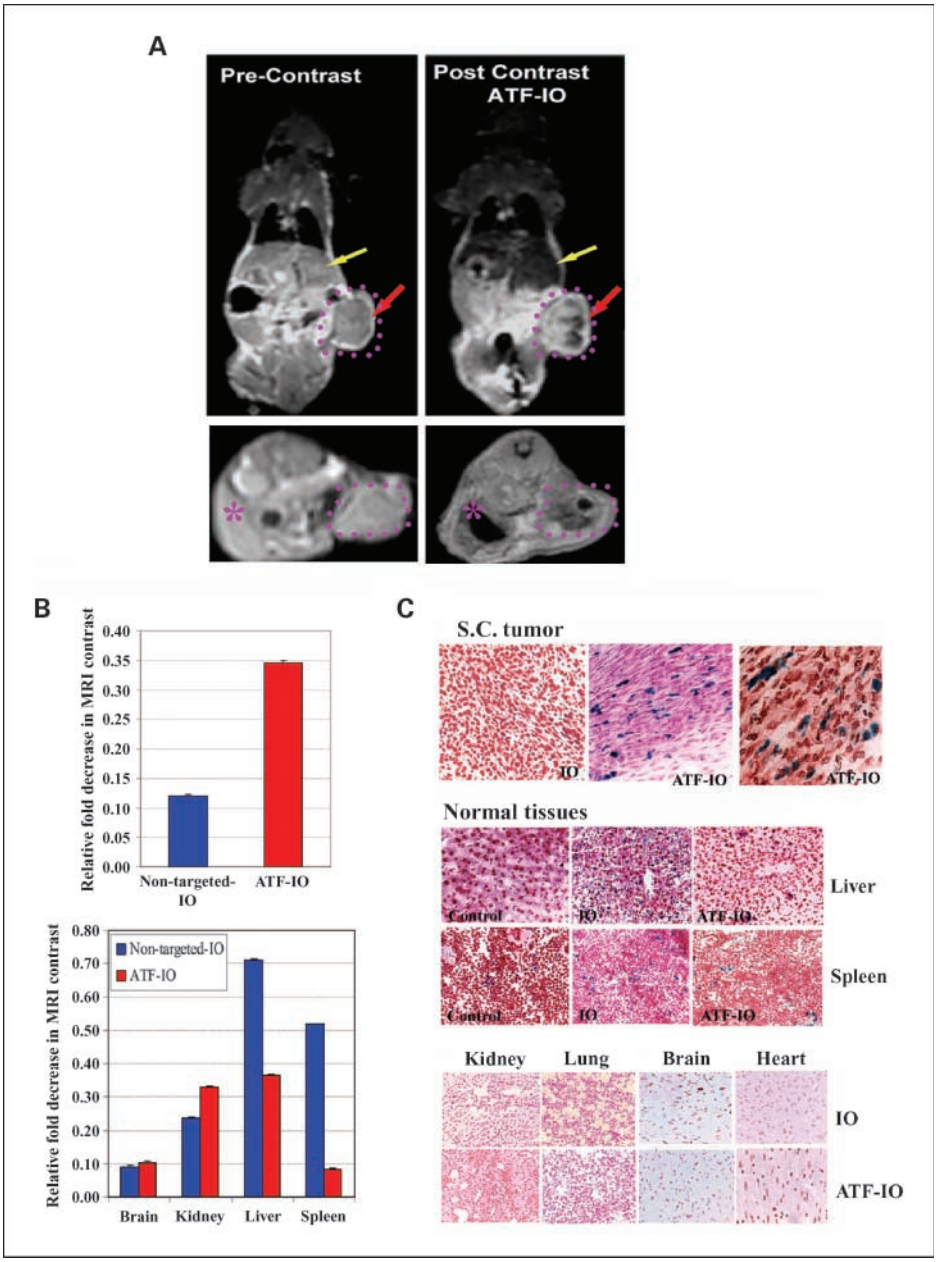

Fig. 4. *In vivo* magnetic resonance imaging of 4T1 mammary tumor using ATF-IO nanoparticles. *A,* magnetic resonance imaging of s.c. mammary tumor. A marked magnetic resonance imaging signal drop with T_2 weighted contrast was observed in s.c. tumor areas (*pink dashed lined*) 6 h after the tail vein ATF-IO nanoparticles. Heterogeneous signal changes suggest that intratumoral distribution of ATF-IO nanoparticles is not uniform in the s.c. tumor (*red arrow*). T_2 contrast change is also found in the liver (*yellow arrows* and *pink asterisk*). Selected magnetic resonance image is a representative image of seven mice that received ATF-IO nanoparticles. A magnetic resonance image of the mouse that received nontargeted iron oxide nanoparticles is in Fig. 6B. *B,* organ-specific profiling of magnetic resonance imaging signal change. Signal changes in the mice that received nontargeted iron oxide or ATF-IO nanoparticles for 6 h were measured in the regions of tumor or various normal tissues. Relative intensity was calculated using the intensity in the leg muscle as a reference. Fold decreases in the intensity of the magnetic resonance image were compared between pre– and post–ATF-IO nanoparticle injections and plotted in the figure. Bar plot, mean values of three regions. *C,* Prussian blue staining of the iron oxide nanoparticles in tumor and normal tissues 48 h after injection of the nanoparticles. Red, background staining with nuclear fast red.

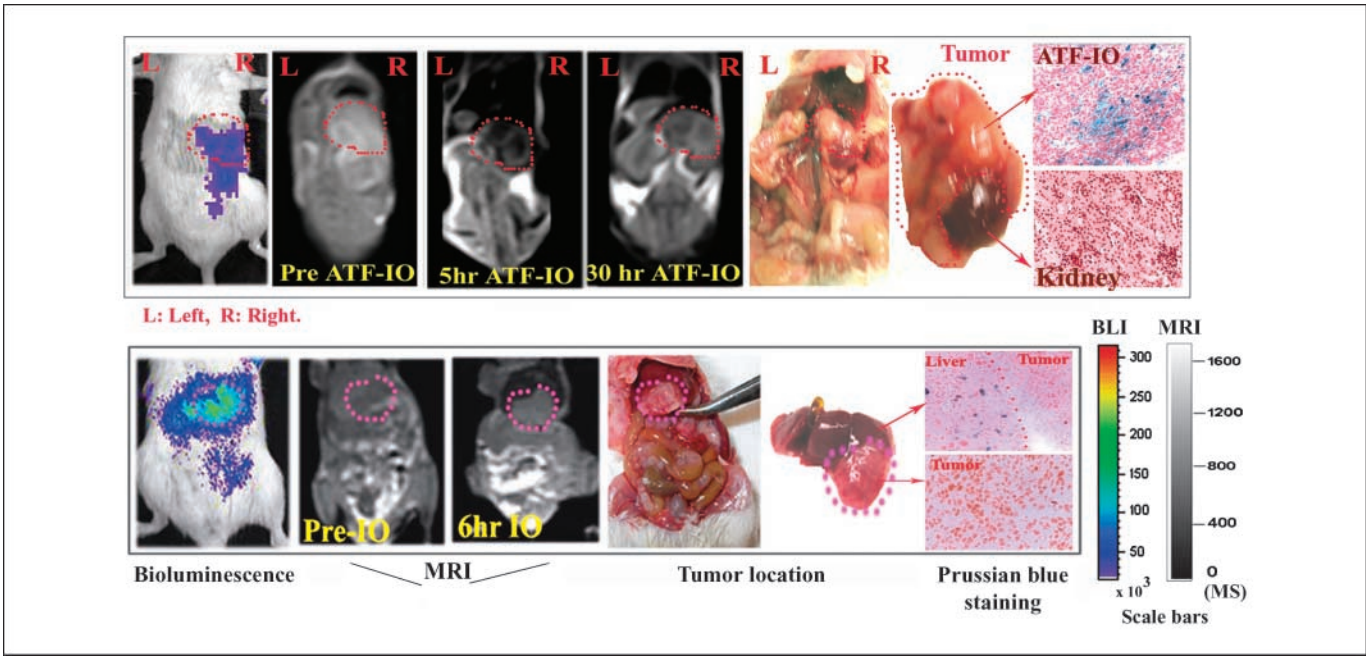

Fig. 5. Targeting and *in vivo* magnetic resonance tumor imaging of i.p. mammary tumor lesions. Top, bioluminescence imaging detects the presence of i.p. tumors on the upper right of the peritoneal cavity of the mouse. Magnetic resonance images reveal two areas located near the right kidney (*red dashed lined*) with decreased magnetic resonance imaging signals 5 or 30 h after the tail vein injection of 11.2 nmol/kg of body weight of ATF-IO nanoparticles, which corresponded to the locations detected by bioluminescence imaging. Examination of the mouse peritoneal cavity confirmed the locations of two tumor lesions on the top of the right kidney. Specific accumulation of ATF-IO nanoparticles in the tumor tissues was confirmed by Prussian blue staining. Bottom, the control mouse with a tumor lesion in the upper right of the peritoneal cavity received nontargeted iron oxide (IO) nanoparticles. There is no magnetic resonance imaging contrast change in the tumor area (*pink dashed lined*) 6 h after administration of iron oxide nanoparticles, whereas the liver of the mouse shows a marked contrast decrease. Prussian blue staining of tissue sections revealed iron-positive cells in the normal liver near the tumor region but not in the tumor tissues (A red dashed line divides normal liver and tumor tissue areas).

intratumoral distribution of the targeted nanoparticles varies in different areas (Fig. 6C). Interestingly, areas with the greatest decline in signal were largely in the periphery regions of the tumor mass, which are rich in blood vessels relative to the necrotic areas at the center of the tumor.

Discussion

Molecular imaging probes targeting specific cancer markers have been long sought after in applying tumor imaging for disease-specific detection and personalized therapeutics. However, the development of receptor-targeted imaging and its *in vivo* applications are particularly challenging, with current obstacles including (*a*) the identification of cell-surface biomarkers that are expressed sufficiently in tumor cells or tumor environments for sensitive tumor imaging, (*b*) the production of stable and high-affinity targeting ligands in large amounts for *in vivo* studies, and (*c*) the development of safe and biodegradable contrast agents that can also produce strong imaging signal or contrast.

The uPA receptor–targeted iron oxide nanoparticle probe reported here provides an example that addresses these challenges and shows the feasibility of *in vivo* receptor-targeted tumor imaging with MRI at clinical field strength. Results of our study showed that amino-terminal fragment–iron oxide nanoparticles are capable of targeting uPA receptor–expressing tumor cells *in vitro* and *in vivo* and enable receptor-targeted magnetic resonance and optical imaging of the tumor *in vivo*. We believe that the following characteristics of amino-terminal fragment–iron oxide nanoparticles enabled uPA receptor–targeted imaging *in vivo*. First, we used a tumor-targeting ligand from a natural high-affinity receptor-binding domain of uPA. uPA is composed

Fig. 6. Dual modality imaging of s.c. 4T1 mouse mammary tumor using Cy5.5– ATF-IO nanoparticles. *A,* near-IR optical imaging of tumor targeting and tissue distribution of Cy5.5– ATF-IO nanoparticles over time. A nude mouse bearing an s.c. 4T1 tumor received 200 pmol per mouse of Cy5.5– ATF-IO nanoparticles in 50 μL PBS, which was calculated from the iron oxide nanoparticle concentration. Near-IR optical imaging was done at different time points. Pink arrows, s.c. tumor; green arrows, kidneys. Back and side images are at 72 h. *B,* simultaneous magnetic resonance and optical imaging of mammary tumor. A tumor-bearing mouse received Cy5.5– ATF-IO nanoparticles showed a signal drop after 48 h in the lower-left half of the s.c. tumor in T_2-weighted magnetic resonance image. Optical imaging reveals the near-IR signal in the tumor area corresponding well with the magnetic resonance imaging results (*bottom, pink dashed lined*). T_2 contrast change is not detected in the s.c. tumor of the mouse that received nontargeted iron oxide nanoparticles (*top*). Magnetic resonance image is the results of a total of seven control tumor-bearing mice that received iron oxide nanoparticles. *C,* examination of the location of ATF-IO nanoparticles and Cy5.5 signal in tumor tissues. Double labeling of Prussian blue staining and an Alexa Fluor 488– anti-CD68 antibody reveals that many blue iron-positive cells are negative for CD68 (*red arrow*). Moreover, colocalization of iron staining and Cy5.5 signal is also detected in the tumor tissues (*white arrows*). *D,* T_2 map of a series of magnetic resonance images taken from an s.c. mammary tumor lesion using multi-echo T_2-weighted spin echo magnetic resonance imaging. Top, control magnetic resonance images taken before ATF-IO nanoparticle injection. Bottom, corresponding magnetic resonance images taken 48 h after injection of ATF-IO nanoparticles. Orange-to-red colored areas, tumor areas with the greatest reduction of T_2 relaxation time. Regional of interest analysis of T_2 mapping was used. T_2 map typically was obtained for the whole mouse, but only the tumor as region of interest was displayed here to present an overlay of T_2 values with anatomic images.

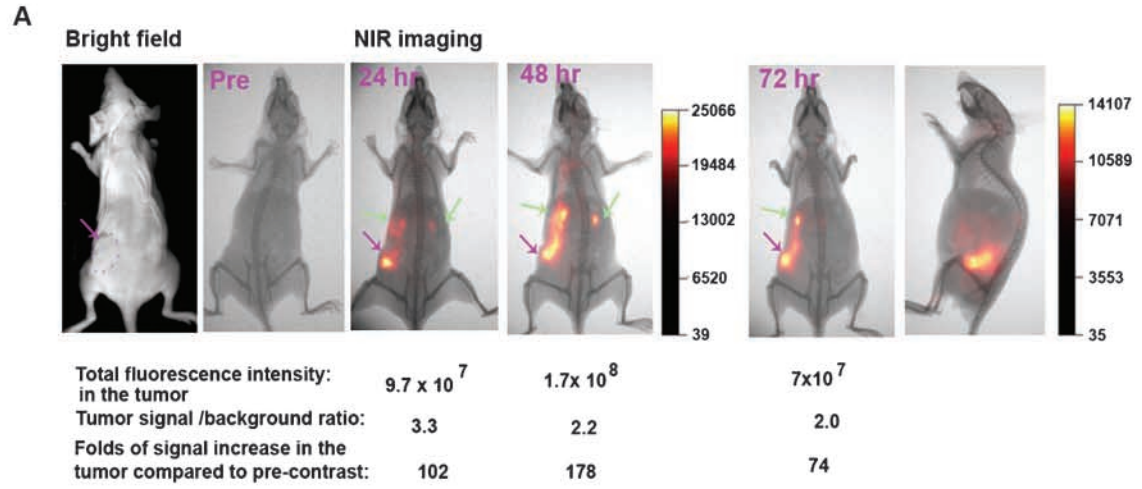

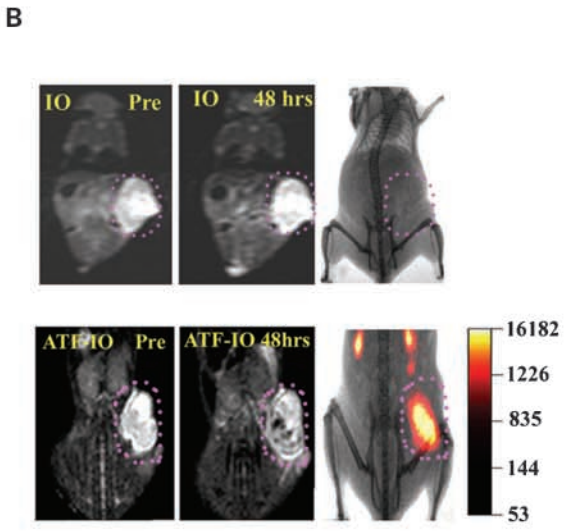

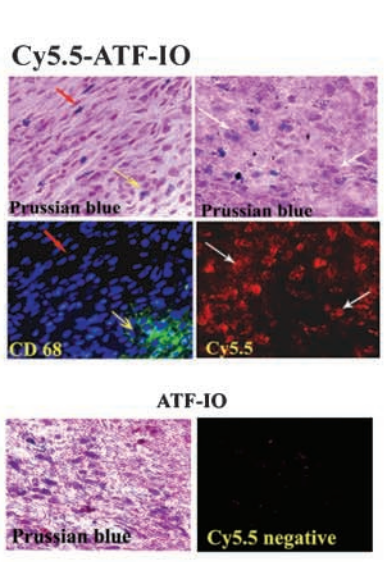

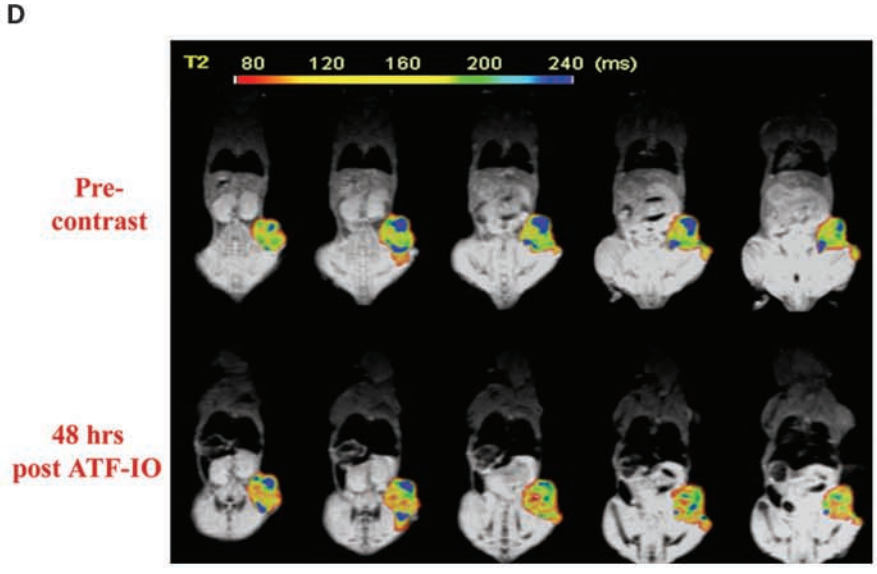

of three independently folded domain structures: growth factor domain, Kringle domain, and serine protease domain. uPA binds with high affinity to uPA receptor through the amino-terminal fragment of the growth factor domain, with a dissociation constant (Kd) < 1 nmol/L (39). Studies have shown that amino-terminal fragment (residues 1-135 amino acid) of uPA is a potent antagonist of uPA/uPA receptor binding because amino-terminal fragment lacks the serine protease domain of uPA, which negatively regulates its function by cleaving uPA receptor into a nonbinding receptor (40, 41). Second, efficient internalization of the ligand/receptor complex may increase the concentration of the iron oxide nanoparticles in tumor cells, which enhances the effect of uPA receptor–targeted tumor imaging (35, 42). Third, nanoparticles provide favorable pharmacokinetics by prolonging blood circulation time, allowing sufficient amounts of nanoparticles to reach the tumor. Furthermore, our ability to produce the recombinant protein in a large scale is essential for preclinical and eventually clinical studies. It should be mentioned that this study was done using mouse amino-terminal fragment peptides and the 4T1 mouse tumor model to investigate the feasibility of targeting uPA receptor. Although it has been shown that the interaction of uPA with its receptor has species specificity (43), we found that mouse amino-terminal fragment peptides bind efficiently to mouse tumor cells and also show cross-reactivity with human uPA receptor–expressing tumor cells. A major advantage of using mouse amino-terminal fragment peptides to conduct studies in a mouse tumor model is that the targeting specificity and biodistribution in normal tissues of this imaging probe can be studied in greater detail. For future clinical application, it is desirable to use a human amino-terminal fragment peptide. We have produced recombinant human amino-terminal fragment peptides and have shown target specificity in human breast cancer xenograft models in nude mice.[7]

Extensive studies have shown that human breast cancer and tumor stromal cells have a much higher level of uPA receptor compared with normal breast tissues (44, 45). Differences between the level of uPA receptor present on the surface of normal and tumor cells suggest that an elevated uPA receptor in cancer may be sufficient for *in vivo* uPA receptor–targeted tumor imaging. Several studies have shown that the highest level of uPA receptor expression is detected in the invasive edge of the tumor regions (23, 28), which are usually enriched in blood vessels, making this area particularly accessible for uPA receptor–targeted iron oxide nanoparticles. In addition, the ability of nanoparticles to leak across tumor endothelium but not normal vasculatures by passive targeting may prevent the interaction of targeted nanoparticles with some cell types in normal tissues that express a low level of uPA receptor.

In this study, we prepared high-quality and uniformly sized iron oxide nanoparticles with a thin ampiphilic copolymer coating (estimated at 2 nm). Compared with conventional dextran or polyethylene glycol-coated nanoparticles used previously, ampiphilic copolymer–coated iron oxide nanoparticles form a relatively small particle complex (~ 18 nm in this study), which is desirable for *in vivo* delivery of the imaging probe. Several previous studies used a commercially available superparamagnetic iron oxide nanoparticle, Feridex, which has a particle core size distribution of 20 to 30 nm or 80 to 150 nm in overall diameter with dextran coating (13). We believe that size uniformity is essential for potential quantification using magnetic resonance imaging signal of the amount of probe *in vivo*.

Although other small molecule imaging agents may have better intratumoral distribution than nanoparticle-based imaging agents, these imaging agents are usually eliminated from the blood circulation in a relatively short time (<30 minutes), which makes it unlikely that sufficient levels of the targeted contrast agents can accumulate at the tumor site (2). It has been shown that polymer-coated iron oxide nanoparticles have >8 hours of plasma retention time (11). This longer circulation time could be an important factor enabling targeted iron oxide nanoparticles to reach the tumor site and bind to tumor cells. amino-terminal fragment–iron oxide nanoparticles were stable *in vivo* and in intracellular environments for >48 hours during our imaging experiments. We observed that the intratumoral near-IR signal increased over time and reached its highest level around 48 hours after the administration of iron oxide nanoparticles, suggesting that the long blood retention time may facilitate nanoparticle tumor targeting.

It has been reported by several other groups that large proportions of magnetic iron oxide nanoparticles are taken up by the reticuloendothelial system in the liver and spleen and then are subsequently metabolized or used for iron storage (12, 13). Our data showed that amino-terminal fragment–iron oxide nanoparticles have reduced liver and spleen uptake compared with nontargeted iron oxide nanoparticles. This suggests that conjugation of amino-terminal fragment-peptides to the iron oxide nanoparticles attenuates their nonspecific capture and retention in the liver and spleen, which commonly occurs after systemic delivery.

In conclusion, we have developed a uPA receptor–targeted molecular imaging nanoprobe that has a uniform-sized iron oxide nanocrystal core, a thin ampiphilic copolymer coating, and a high affinity receptor binding domain of uPA conjugated with a near-IR dye. This receptor-targeted nanoprobe selectively binds to and is internalized by tumor cells and can specifically accumulate in primary and metastatic tumors, facilitating *in vivo* magnetic resonance and optical imaging in a mouse mammary tumor model. Such uPA receptor–targeted imaging nanoparticles are promising probes for molecular magnetic resonance imaging of breast cancer and several other cancer types, such as pancreatic, lung, and brain, which express high levels of uPA receptor (46–48). Given that chemotherapy drugs can be incorporated into the targeted nanoparticles (49), it will be feasible to use uPA receptor–targeted iron oxide nanoparticles for delivery of therapeutic agents into tumor cells and monitoring the response to therapy using magnetic resonance imaging.

Disclosure of Potential Conflicts of Interest

No potential conflicts of interest were disclosed.

Acknowledgments

We thank Dr. Anthea Hammond for her critical editing of the manuscript, Dr. Mark W. Dewhirst for kindly providing us with luciferase gene – stable 4T1 cell line, Drs. Adam Marcus and Katherine Schafer-Hales in the Cell Imaging Core of the Winship Cancer Institute for their assistance in confocal microscopy, and Dr. Hongwei Duan for his help with zeta potential and particle size analysis.

[7] H. Sajja, Z. Cao, and L. Yang, unpublished observation.

References

1. Weissleder R. Molecular imaging in cancer. Science 2006;312:1168–71.
2. Massoud TF, Gambhir SS. Molecular imaging in living subjects: seeing fundamental biological processes in a new light. Genes Dev 2003;17:545–80.
3. Artemov D, Mori N, Ravi R, Bhujwalla ZM. Magnetic resonance molecular imaging of the HER-2/*neu* receptor. Cancer Res 2003;63:2723–7.
4. Hofmann M. From scinti-mammography and metabolic imaging to receptor targeted PET—new principles of breast cancer detection. Phys Med 2006;21:11.
5. Benard F, Turcotte E. Imaging in breast cancer: single-photon computed tomography and positron-emission tomography. Breast Cancer Res 2005;7:153–62.
6. Saslow D, Boetes C, Burke W, et al. American Cancer Society guidelines for breast screening with MRI as an adjunct to mammography. CA Cancer J Clin 2007;57:75–89.
7. Hede K. Possible MRI-mastectomy link sparks debate on MRI's role in breast cancer management. J Natl Cancer Inst 2008;100:1052–4.
8. Nasongkla N, Bey E, Ren J, et al. Multifunctional polymeric micelles as cancer-targeted, MRI-ultrasensitive drug delivery systems. Nano Lett 2006;6:2427–30.
9. Sukhorukov GB, Rogach AL, Garstka M, et al. Multifunctionalized polymer microcapsules: novel tools for biological and pharmacological applications. Small 2007;3:944–55.
10. Medarova Z, Pham W, Farrar C, Petkova V, Moore A. *In vivo* imaging of siRNA delivery and silencing in tumors. Nat Med 2007;13:372–7.
11. Moore A, Marecos E, Bogdanov A, Jr., Weissleder R. Tumoral distribution of long-circulating dextran-coated iron oxide nanoparticles in a rodent model. Radiology 2000;214:568–74.
12. Bulte JW, Kraitchman DL. Iron oxide MR contrast agents for molecular and cellular imaging. NMR Biomed 2004;17:484–99.
13. Thorek DL, Chen AK, Czupryna J, Tsourkas A. Superparamagnetic iron oxide nanoparticle probes for molecular imaging. Ann Biomed Eng 2006;34:23–38.
14. Lee JH, Huh YM, Jun YW, et al. Artificially engineered magnetic nanoparticles for ultra-sensitive molecular imaging. Nat Med 2007;13:95–9.
15. Schultz JF, Bell JD, Goldstein RM, Kuhn JA, McCarty TM. Hepatic tumor imaging using iron oxide MRI: comparison with computed tomography, clinical impact, and cost analysis. Ann Surg Oncol 1999;6:691–8.
16. Harisinghani MG, Barentsz J, Hahn PF, et al. Noninvasive detection of clinically occult lymph-node metastases in prostate cancer. N Engl J Med 2003;348:2491–9.
17. Choi H, Choi SR, Zhou R, Kung HF, Chen IW. Iron oxide nanoparticles as magnetic resonance contrast agent for tumor imaging via folate receptor-targeted delivery. Acad Radiol 2004;11:996–1004.
18. Medarova Z, Pham W, Kim Y, Dai G, Moore A. *In vivo* imaging of tumor response to therapy using a dual-modality imaging strategy. Int J Cancer 2006;118:2796–802.
19. Simberg D, Duza T, Park JH, et al. Biomimetic amplification of nanoparticle homing to tumors. Proc Natl Acad Sci U S A 2007;104:932–6.
20. Blasi F, Carmeliet P. uPAR: a versatile signalling orchestrator. Nat Rev Mol Cell Biol 2002;3:932–43.
21. Hildenbrand R, Wolf G, Bohme B, Bleyl U, Steinborn A. Urokinase plasminogen activator receptor (CD87) expression of tumor-associated macrophages in ductal carcinoma *in situ*, breast cancer, and resident macrophages of normal breast tissue. J Leukoc Biol 1999;66:40–9.
22. Duffy MJ. The urokinase plasminogen activator system: role in malignancy. Curr Pharm Des 2004;10:39–49.
23. Dublin E, Hanby A, Patel NK, Liebman R, Barnes D. Immunohistochemical expression of uPA, uPAR, and PAI-1 in breast carcinoma. Fibroblastic expression has strong associations with tumor pathology. Am J Pathol 2000;157:1219–27.
24. Duggan C, Maguire T, McDermott E, O'Higgins N, Fennelly JJ, Duffy MJ. Urokinase plasminogen activator and urokinase plasminogen activator receptor in breast cancer. Int J Cancer 1995;61:597–600.
25. Guyton DP, Evans DM, Sloan-Stakleff KD. Urokinase plasminogen activator receptor (uPAR): a potential indicator of invasion for *in situ* breast cancer. Breast J 2000;6:130–6.
26. Fisher JL, Field CL, Zhou H, Harris TL, Henderson MA, Choong PF. Urokinase plasminogen activator system gene expression is increased in human breast carcinoma and its bone metastases—a comparison of normal breast tissue, non-invasive and invasive carcinoma and osseous metastases. Breast Cancer Res Treat 2000;61:1–12.
27. Giannopoulou I, Mylona E, Kapranou A, et al. The prognostic value of the topographic distribution of uPAR expression in invasive breast carcinomas. Cancer Lett 2007;246:262–7.
28. Hemsen A, Riethdorf L, Brunner N, et al. Comparative evaluation of urokinase-type plasminogen activator receptor expression in primary breast carcinomas and on metastatic tumor cells. Int J Cancer 2003;107:903–9.
29. Han B, Nakamura M, Mori I, Nakamura Y, Kakudo K. Urokinase-type plasminogen activator system and breast cancer [review]. Oncol Rep 2005;14:105–12.
30. Yu WW, Falkner JC, Yavuz CT, Colvin VL. Synthesis of monodisperse iron oxide nanocrystals by thermal decomposition of iron carboxylate salts. Chem Commun (Camb) 2004:2306–7.
31. Gao X, Cui Y, Levenson RM, Chung LW, Nie S. *In vivo* cancer targeting and imaging with semiconductor quantum dots. Nat Biotechnol 2004;22:969–76.
32. Yang L, Cao Z, Yan H, Wood WC. Coexistence of high levels of apoptotic signaling and inhibitor of apoptosis proteins in human tumor cells: implication for cancer specific therapy. Cancer Res 2003;63:6815–24.
33. Frank JA, Miller BR, Arbab AS, et al. Clinically applicable labeling of mammalian and stem cells by combining superparamagnetic iron oxides and transfection agents. Radiology 2003;228:480–7.
34. Bulte JW, Vymazal J, Brooks RA, Pierpaoli C, Frank JA. Frequency dependence of MR relaxation times. II. Iron oxides. J Magn Reson Imaging 1993;3:641–8.
35. Vilhardt F, Nielsen M, Sandvig K, van Deurs B. Urokinase-type plasminogen activator receptor is internalized by different mechanisms in polarized and nonpolarized Madin-Darby canine kidney epithelial cells. Mol Biol Cell 1999;10:179–95.
36. Soling A, Rainov NG. Bioluminescence imaging *in vivo*—application to cancer research. Expert Opin Biol Ther 2003;3:1163–72.
37. Lewis JS, Landers RJ, Underwood JC, Harris AL, Lewis CE. Expression of vascular endothelial growth factor by macrophages is up-regulated in poorly vascularized areas of breast carcinomas. J Pathol 2000;192:150–8.
38. Nielsen BS, Rank F, Illemann M, Lund LR, Dano K. Stromal cells associated with early invasive foci in human mammary ductal carcinoma *in situ* coexpress urokinase and urokinase receptor. Int J Cancer 2007;120:2086–95.
39. Ploug M, Ellis V. Structure-function relationships in the receptor for urokinase-type plasminogen activator. Comparison to other members of the Ly-6 family and snake venom alpha-neurotoxins. FEBS Lett 1994;349:163–8.
40. Hoyer-Hansen G, Ploug M, Behrendt N, Ronne E, Dano K. Cell-surface acceleration of urokinase-catalyzed receptor cleavage. Eur J Biochem 1997;243:21–6.
41. Li H, Soria C, Griscelli F, et al. Amino-terminal fragment of urokinase inhibits tumor cell invasion *in vitro* and *in vivo*: respective contribution of the urokinase plasminogen activator receptor-dependent or -independent pathway. Hum Gene Ther 2005;16:1157–67.
42. Rajagopal V, Kreitman RJ. Recombinant toxins that bind to the urokinase receptor are cytotoxic without requiring binding to the alpha(2)-macroglobulin receptor. J Biol Chem 2000;275:7566–73.
43. Quax PH, Grimbergen JM, Lansink M, et al. Binding of human urokinase-type plasminogen activator to its receptor: residues involved in species specificity and binding. Arterioscler Thromb Vasc Biol 1998;18:693–701.
44. Del Vecchio S, Stoppelli MP, Carriero MV, et al. Human urokinase receptor concentration in malignant and benign breast tumors by *in vitro* quantitative autoradiography: comparison with urokinase levels. Cancer Res 1993;53:3198–206.
45. Li Y, Wood N, Yellowlees D, Donnelly PK. Cell surface expression of urokinase receptor in normal mammary epithelial cells and breast cancer cell lines. Anticancer Res 1999;19:1223–8.
46. Cantero D, Friess H, Deflorin J, et al. Enhanced expression of urokinase plasminogen activator and its receptor in pancreatic carcinoma. Br J Cancer 1997;75:388–95.
47. Pedersen H, Brunner N, Francis D, et al. Prognostic impact of urokinase, urokinase receptor, and type 1 plasminogen activator inhibitor in squamous and large cell lung cancer tissue. Cancer Res 1994;54:4671–5.
48. Yamamoto M, Sawaya R, Mohanam S, et al. Expression and localization of urokinase-type plasminogen activator receptor in human gliomas. Cancer Res 1994;54:5016–20.
49. Yang L, Cao Z, Sajja HK, et al. Development of receptor targeted magnetic iron oxide nanoparticles for efficient drug delivery and tumor imaging J Biomed Nanotech 2008;4:439–49.